CaBLAM! A high-contrast bioluminescent Ca^{2+} indicator derived from an engineered *Oplophorus gracilirostris* luciferase

Gerard G. Lambert[1,*], Emmanuel L. Crespo[2,*], Jeremy Murphy[3,*], Daniela Boassa[1], Selena Luong[4], Dmitrijs Celinskis[3], Stephanie Venn[2], Daniel K. Nguyen[4], Junru Hu[5], Brittany Sprecher[1], Maya O. Tree[2], Richard Orcutt[1], Daniel Heydari[1], Aidan B. Bell[4], Albertina Torreblanca-Zanca[1], Ali Hakimi[6], Diane Lipscombe[2], Christopher I. Moore[3], Ute Hochgeschwender[2], and Nathan C. Shaner[1,‡]

[*]*These authors contributed equally to this work.*

[1]Department of Neurosciences, University of California San Diego School of Medicine, La Jolla, CA USA
[2]College of Medicine, Central Michigan University, Mt. Pleasant, MI USA
[3]Carney Institute for Brain Sciences, Department of Neuroscience, Brown University, Providence, RI USA
[4]University of California San Diego, La Jolla, CA USA
[5]National Center for Microscopy and Imaging Research, University of California San Diego, La Jolla, CA USA
[6]Scintillon Institute, San Diego, CA USA

[‡]Correspondence to ncshaner@health.ucsd.edu

Abstract

Ca^{2+} plays many critical roles in cell physiology and biochemistry, leading researchers to develop a number of fluorescent small molecule dyes and genetically encodable probes that optically report changes in Ca^{2+} concentrations in living cells. Though such fluorescence-based genetically encoded Ca^{2+} indicators (GECIs) have become a mainstay of modern Ca^{2+} sensing and imaging, bioluminescence-based GECIs—probes that generate light through oxidation of a small-molecule by a luciferase or photoprotein—have several distinct advantages over their fluorescent counterparts. Bioluminescent tags do not photobleach, do not suffer from nonspecific autofluorescent background, and do not lead to phototoxicity since they do not require the extremely bright extrinsic excitation light typically required for fluorescence imaging, especially with 2-photon microscopy. Current BL GECIs perform poorly relative to fluorescent GECIs, producing small changes in bioluminescence intensity due to high baseline signal at resting Ca^{2+} concentrations and suboptimal Ca^{2+} affinities. Here, we describe the development of a new bioluminescent GECI, "CaBLAM," which displays much higher contrast (dynamic range) than previously described bioluminescent GECIs and has a Ca^{2+} affinity suitable for capturing physiological changes in cytosolic Ca^{2+} concentration. Derived from a new variant of *Oplophorus gracilirostris* luciferase with superior in vitro properties and a highly favorable scaffold for insertion of sensor domains, CaBLAM allows for single-cell and subcellular resolution imaging of Ca^{2+} dynamics at high frame rates in cultured neurons and *in vivo*. CaBLAM marks a significant milestone in the GECI timeline, enabling Ca^{2+} recordings with high spatial and temporal resolution without perturbing cells with intense excitation light.

Introduction

Genetically encoded Ca^{2+} indicators (GECIs) play a central role in modern biomedical research, with much of our current understanding of systems neuroscience based on Ca^{2+} imaging. GECIs based on FPs have been the subject of intense engineering efforts for decades, leading to continual improvements to the practical properties of this class of biosensor[1–4]. The GCaMP family of GECIs is currently in its eighth revision[5], with improvements in brightness, sensitivity, and response kinetics continuing to be achieved, and new families of FP-based GECIs continue to push the boundaries of performance[6–9]. Bioluminescence (BL)-based GECIs originated with the *A. victoria* photoprotein aequorin[10–12] and, more recently, luciferase-based BL GECIs have been developed by several groups[13–18], but to date none of these BL GECIs have demonstrated imaging performance remotely comparable to highly optimized FP-based GECIs such as the GCaMP series. Specifically, existing BL GECIs, though often bright enough to image at high framerates, display low contrast between resting and active Ca^{2+} concentrations in cells, especially *in vivo,* limiting their use to observing Ca^{2+} dynamics mainly at the population level. This is due mainly to the high baseline BL emission and often suboptimal Ca^{2+} affinity of these indicators.

Here, we describe the development of a variant of *Oplophorus gracilirostris*[19–21] luciferase (OLuc) engineered to provide increased BL emission *in vitro* along with improved folding and performance in protein fusions. The *in vitro* activity improvement of this variant does not correlate with its observed bioluminescent output in cultured cells, suggesting that diffusion of furimazine (Fz) molecules across the plasma membrane may currently limit the

per-molecule light emission achievable with this class of probes. We found that these new variants of OLuc were highly amenable to sensor domain insertion, making them a favorable scaffold for engineering a BL GECI, "CaBLAM," ("Ca^{2+} BioLuminescence Activity Monitor"). We generated CaBLAM variants exhibiting very high contrast and optimized Ca^{2+} affinity useful for imaging Ca^{2+} dynamics in the cytosol of living cells at high frame rates. The directed evolution process for the luciferase focused on maintaining high brightness while improving solubility of fusions. Optimization of the C-terminal peptide sequence was a critical component of both luciferase and GECI engineering and was particularly important for obtaining the high contrast currently unique to CaBLAM.

The luciferase, "SSLuc" ("Sensor Scaffold Luciferase"), is several-fold more active than NanoLuc *in vitro* using Promega's proprietary Fz substrate and is less prone to aggregation than NanoLuc when fused to other proteins, but paradoxically does not appear brighter in mammalian cells. The BL GECI, CaBLAM has similar maximum light output to other described BL GECIs in cells and displays a ~97-fold full-range contrast *in vitro* and up to 15-20-fold in live cultured cells in response to physiological changes in cytosolic Ca^{2+} levels. We further demonstrate that CaBLAM can be effectively imaged at up to 10Hz in cultured primary neurons on a typical widefield microscope and EMCCD camera and can reliably report the Ca^{2+} signal from a field stimulation equivalent to a single action potential. We anticipate that these probes will enable a much wider array of researchers to harness the unique advantages of BL for imaging, sensing, and integrating biological activities.

Results

Rational design and directed evolution of high-activity soluble OLuc variants

We initially set out to develop a variant of OLuc that could efficiently utilize CTZ, reasoning that NanoLuc was only one of the possible endpoints achievable through directed evolution of this lineage of luciferases. Starting from the OLuc mutant eKAZ[22], we performed multiple rounds of directed evolution consisting of alternating error-prone and site-directed mutagenesis libraries in *E. coli*. For each round, variants were selected based on higher bioluminescent emission and solubility. Subsequent engineering of the intact luciferase included the generation of mNeonGreen[23] fusions for enhancement of emission quantum yield, incorporation of a subset of mutations found in NanoLuc[24] and NanoBit[25], optimization of the C-terminal peptide sequence, and fine-tuning interactions between the C-terminal peptide and the rest of the protein. The final clone, which we named SSLuc ("Sensor Scaffold Luciferase", **Fig. 1A**), can be extracted with nearly 100% efficiency from *E. coli* cultures, retains activity *in vitro* over longer storage periods than NanoLuc, and appears to behave more like a monomer in mammalian cells than NanoLuc. Contrary to our original intentions, SSLuc performs best using Fz as its luciferin, though its activity with other CTZ analogs is also higher than we measure for NanoLuc. Interestingly, we found that SSLuc does not appear brighter in mammalian cells than NanoLuc, despite its high performance *in vitro*, suggesting that availability of the luciferin substrate (e.g., Fz) may limit SSLuc's maximum brightness in cells. SSLuc proved to be a favorable luciferase scaffold from which to generate biosensors, and led us to develop a novel high-performance BL GECI, as described below. A detailed account of our development and

characterization of SSLuc can be found in **Supplementary Results and Discussion, Supplementary Table 1, and Supplementary Figures 1-3**.

Development and evaluation of a high-contrast BL GECI

We next explored the design of new BL GECI architectures based on SSLuc. Since the related split luciferase NanoBit[25] was specifically developed as a *reversible* complementation system, we chose the loop between the last two beta strands of the luciferase domain of SSLuc as our split point for insertion of sensor domains, with the goal of generating indicators with a large change in BL output between low and high cytosolic Ca^{2+} concentrations (i.e. [Ca^{2+}] between ~100nM and ~1μM). We trialed several topologies for the sensor, including circularly permuted variants and simple sensor domain insertions of RS20-Calmodulin (RS20-CaM), CaM-RS20, and Troponin C (**Supp Fig. 4**). All versions of the initial GECI displayed readily measurable and fairly large changes in BL between Ca^{2+}-free and high-Ca^{2+} conditions *in vitro*, with the highest contrast consistently observed from variants with RS20 followed by CaM inserted before the C-terminal luciferase peptide (**Fig 1A, B**). Contemporaneously with our exploration of all these topologies, an analogous RS20-CaM configuration was also identified by Farhana et al[14], in which the insertion is an entire GCaMP sensor domain, including the circularly permuted GFP component. In our designs, the fluorescent protein, if present, remains fixed at the N terminus of the luciferase as a FRET partner to enhance the quantum yield of emission[16,17,26,27], and the Ca^{2+}-sensitive signal is restricted to the BL channel, not both channels, unlike GLICO's bimodal signal. Despite this substantial difference and the use of the SSLuc scaffold rather than NanoBit, we found that the tripeptide linker sequences flanking the sensor domains of GLICO were suitable for our new GECI designs as well, and so we adopted these in our final design.

Unexpectedly, the initial clones of our novel BL GECI lineage displayed Ca^{2+} affinities far too high to be practical in living cells, often with K_D < 10nM [Ca^{2+}]. We explored several ways of altering the affinity, including the use of alternate RS20 and CaM sequences derived from existing fluorescent GECIs[28–30] and lower-affinity designed variants of the RS20/CaM pair[31], altering the linker length and composition between the RS20 and CaM, altering linker lengths and compositions between the luciferase and sensor domain, and rational directed mutations to the CaM domain's EF-hand motifs. This combination approach allowed us to select for the brightest clones while also determining which design factors influenced the Ca^{2+} affinity. Ultimately, the best balance of brightness, affinity, and Hill coefficient was achieved using the CaM and RS20 sequences from GCaMP6s coupled with a single point mutation (N98I in full-length calmodulin) chosen from among several naturally occurring mutations in human calmodulins leading to heart rhythm defects[32], producing apparent Ca^{2+} binding affinities around 500nM. This K_D target was selected to align the most sensitive part of the GECI's response curve with a physiologically relevant range of Ca^{2+} concentrations—for example, Ca^{2+} concentrations in the cytosol of rat CA1 hippocampal pyramidal neurons in slices have been measured using small molecule dyes[33] and are estimated to range from 32-59nM when resting and up to >300nM in response to a single action potential. The process of evaluating the many variables contributing to the calcium-binding behavior of this BL GECI architecture

generated multiple related BL GECI variants suitable for future optimization and engineering for specific biological use cases requiring higher and lower Ca^{2+} affinities.

To maximize the BL signal contrast between inactive and active cytosolic Ca^{2+} concentrations, we systematically evaluated variants of the C-terminal SSLuc peptide, initially choosing peptides described from the development of NanoBit[25] as we had previously done during SSLuc optimization. We found that the clones displaying the highest contrast in luciferase activity between low and high [Ca^{2+}] contained the low-affinity peptide **VTGYRLFEEIL** ("pep114"). We then designed peptides based on this core sequence, drawing inspiration from the best-performing peptides identified during the evolution of SSLuc (**Supp. Table 1**). Ultimately, this led us to choose the peptide **VTGYRLLEEISN** for the final variant, which we named "CaBLAM." The rationale for the design of this peptide, which contains two glutamate residues substituted for the preferred lysines in SSLuc, was to maintain enzymatic activity (largely from the arginine side chain that forms part of the putative active site[34]) while also reducing affinity for the large piece of the luciferase to increase the contrast in luciferase activity between the unbound and Ca^{2+}-bound states. We speculate this low affinity allows the C-terminus of the luciferase to disengage from the enzyme more fully under low Ca^{2+} concentrations, decreasing luciferase activity at baseline. *In vitro* characterization of CaBLAM indicated that it has a K_D of ~460nM [Ca^{2+}] and an absolute contrast (i.e., the ratio of luminescence emission between saturating Ca^{2+} and zero Ca^{2+}, typically reported for this class of sensor) of ~97-fold (**Fig. 1C, Table 1**). This value compares favorably to other published BL GECIs, all of which display substantially lower contrast than CaBLAM[14,17,18]. The Hill coefficient of CaBLAM is ~3, similar to that of GeNL(Ca^{2+})_480[17] and notably higher than that of CaMBI[18], which displays a Hill coefficient of ~1.2 in our hands (**Fig. 1C, Table 1**). CaBLAM also has a similar Ca^{2+} affinity to GeNL(Ca^{2+})_480, making these two GECIs a well-matched pair for benchmarking in cells. In practice, when a GECI is expressed in a living system, its contrast drops dramatically compared to *in vitro* values, and so we next evaluated the behavior of CaBLAM in cultured cells in comparison with the published GeNL(Ca^{2+})_480 GECI.

Characterization and evaluation of CaBLAM in cells

We first evaluated CaBLAM variants by widefield imaging of U2OS (human osteosarcoma) cells, which display only small spontaneous changes in cytosolic Ca^{2+} concentration in our hands. CaBLAM consistently generated large changes in BL with ionomycin treatment with a dynamic range 5.4±0.1-fold higher (95% confidence interval (95%CI)) than that of GeNL(Ca^{2+})_480 (**Fig. 2A**). Coupled with the *in vitro* characterization data, these results suggest that the larger contrast for CaBLAM over GeNL(Ca^{2+})_480 in cells is due to the lower baseline luminescence of CaBLAM coupled with its favorable Hill coefficient. The contrast achievable in living cells sets CaBLAM apart from existing BL GECIs, and is expected to enable observation of small changes in Ca^{2+} concentration more readily than is currently possible.

To address some potential shortcomings of ionomycin experiments and observe a physiologically generated Ca^{2+} signal, we next evaluated the performance of CaBLAM in HeLa cells, known to undergo large oscillations in cytosolic Ca^{2+} in response to a number of stimuli[35]. We observed strong asynchronous oscillations in single-cell BL signals over varying time scales in HeLa cells treated with L-histamine. In parallel experiments, we were able

to observe small changes in cells expressing GeNL(Ca^{2+})_480, with a dynamic range 3.3±0.1-fold (95%CI) lower than observed with CaBLAM, consistent with the results of previous ionomycin experiments (**Fig. 2B**). CaBLAM revealed a wide variety of Ca^{2+} oscillation phenotypes in these imaging experiments, with periods ranging from seconds to minutes (**Fig. 2D** and **Supp. Movie 1**).

We compared the high-Ca^{2+} brightness (maximal brightness) of CaBLAM compared with GeNL(Ca^{2+})_480 by normalizing the signal to the mNeonGreen fluorescence signal for each. However, as with SSLuc, we observed an unexpectedly weak correlation between fluorescence and BL brightness in all but the lowest-expressing cells for both GECIs, which we suspect is due to rate-limiting substrate diffusion across the plasma membrane. Analysis of the cells with low expression of each sensor indicates that CaBLAM is ~39% ± 19% as bright as GeNL(Ca^{2+})_480 on a per-molecule basis (95%CI). The uncertainty in this estimate is high due to the weak linear correlation between fluorescence and BL intensity for both indicators, even at low expression levels (**Supp Fig. 5**).

Finally, we evaluated CaBLAM in cultured primary rat cortical neurons to determine whether it was suitable for real-time reporting of depolarization-induced Ca^{2+} influx. Neurons expressing CaBLAM were imaged similarly to the U2OS and HeLa cells in the previous assays, with dark background frames collected followed by injection of Fz diluted in medium, imaging for 60s, then injection of concentrated KCl to give a final extracellular concentration of 30mM KCl. Upon injection of KCl, the neurons were expected to depolarize, opening voltage-gated Ca^{2+} channels and subsequently inducing secondary Ca^{2+} release to the cytosol from the ER. Consistent with previous contrast measurements in cell lines, these neurons generated a ~15-fold increase in BL emission from CaBLAM between resting and depolarized cytosolic Ca^{2+} levels (**Fig 2C**). We performed identical experiments using GeNL(Ca^{2+})_480 and observed a 3.8±0.1-fold lower contrast, consistent with ionomycin and histamine experiments in cell lines.

Comparison of CaBLAM to GCaMP8s in rat hippocampal neurons

We performed simultaneous calcium imaging and electrical field stimulation (FS) to characterize the CaBLAM sensor (**Supp. Movie 2**). To benchmark its performance to report fluctuations in intracellular calcium, we compared it to GCaMP8s, which allowed us to quantify both temporal kinetics and response magnitudes with a state-of-the art sensor. CaBLAM-expressing neurons showed low detectable photon counts during 10 Hz imaging, yet individual traces demonstrated detectable evoked responses across a range of electrical field stimulations (**Fig. 3A** and **C**). As expected for a fluorescent indicator, GCaMP8s was brighter overall and captured both spontaneous and evoked neural activity (**Fig. 3B** and **D**). These initial observations represent typical examples of the responses observed for each indicator. We calculated the evoked change in bioluminescence for CaBLAM, showing that it reliably reported changes in intracellular calcium, with large changes observed in the normalized ($\Delta L/L$) signal (**Fig. 3C**). For GCaMP8s (**Fig. 3D**), the normalized change in fluorescence ($\Delta F/F$) was reduced due to its high baseline fluorescence. Despite this, GCaMP8s still produced observable changes in fluorescence, consistent with previous reports.

We next characterized stimulus-evoked bioluminescence and fluorescence signals in neurons expressing CaBLAM **(Fig. 4A**) and GCaMP8s (**Fig. 4B**). Consistent with our initial observation, electrical field stimulations (1, 5, and 40 pulses at ~83 Hz, 1ms pulse) revealed higher detectable changes in ΔL/L due to the low background signal of CaBLAM when compared to GCaMP8s ΔF/F (**Fig. 4C**, Wilcoxon signed rank sum test, two tailed, Bonferroni correction for multiple comparisons, CaBLAM vs GCaMP8s at 1 FS: $P = 1.1 \times 10^{-10}$, 5 FS: $P = 2.45 \times 10^{-21}$, 60 FS: $P = 2.03 \times 10^{-2}$). The response kinetics of CaBLAM are considerably slower than GCaMP8s, as expected since CaBLAM has not yet been optimized for fast responses (Fig. 2d, two-tailed Kolmogorov-Smirnov test, ($P = 7.1 \times 10^{-51}$, N= 96 trials/20-38 GCaMP8s expressing neurons vs 570 trials/88-276 CaBLAM expressing neurons). For both indicators, we measured the time to peak ΔL/L (CaBLAM) and ΔF/F (GCaMP8s) and observed distinct response timing. GCaMP8s reached peak responses around 100 ms (approximately 1 frame post-stimulation at our 10 Hz imaging rate) for 1 and 5 pulses, while the response extended to 300 ms (about 3 frames) for higher stimulation frequencies (**Fig. 4C,** Wilcoxon signed rank sum test, two tailed, Bonferroni correction for multiple comparisons, CaBLAM vs GCaMP8s at 1 FS: $P = 1.93 \times 10^{-05}$, 5 FS: $P = 1.07 \times 10^{-16}$, 60 FS: $P = 1.24 \times 10^{-22}$). In contrast, CaBLAM under constant Fz perfusion (1x / 1:1 final concentration), displayed median peak response times of approximately 700, 800, and 1500 ms post-stimulation for 1, 5, and 40 pulses, respectively. As these experiments did not include synaptic blockers, the true indicator kinetics are likely faster than measured.

We hypothesized that reducing photon emission by decreasing the amount of Fz at resting calcium levels would lead to larger changes in ΔL/L upon stimulation, thereby enhancing the sensitivity of CaBLAM to report intracellular calcium dynamics. In line with our prediction, neurons expressing CaBLAM in 1:2x Fz reported larger stimulus time-locked responses compared to those in 1:1x bath application of Fz at both lower and higher stimulation levels (**Fig. 5A** and **B**). This suggests an improved ability to detect smaller changes in intracellular calcium in a concentration dependent manner. We pooled all time-locked evoked responses across stimulations to analyze the average response and temporal kinetics of CaBLAM. Decreasing the concentration of constant Fz perfusion led to a reduction in the time to peak ΔL/L for CaBLAM, indicating a faster response at lower Fz concentrations (**Fig. 5C**, two-tailed Kolmogorov-Smirnov test, ($P = 5.61 \times 10^{-8}$, N=333 trials/148 neurons in 1:2x Fz vs 961 trials/322 neurons in 1:1x Fz). Surprisingly, reducing the luciferin substrate concentration not only increased the speed of the sensor but also enhanced the evoked ΔL/L response in the presence of 1:2x Fz (Wilcoxon signed rank sum test, two tailed, Bonferroni correction for multiple comparisons, $P = 6.63 \times 10^{-5}$, 1:2x Fz: Mean= 3.24, Median= 2.49, SD=2.15, 95% CI= [3.01, 3.47], 1:1x Fz: Mean= 2.71, Median= 2.42, SD=1.85, 95% CI= [2.59, 2.83]). These findings are surprising because reducing the luciferin concentration would typically decrease overall signal, obscuring detectable changes in intracellular calcium levels. Unlike fluorescent indicators with high resting fluorescence that reduces the observed ΔF/F, CaBLAM was optimized for low baseline light emission at resting calcium levels, enabling a quantifiable and robust ΔL/L response upon stimulation. Therefore, reducing luciferin substrate concentration improves CaBLAM's performance by increasing both the speed and magnitude of the evoked bioluminescent calcium dependent response.

We then proceeded to compare the *responsiveness* of neurons expressing CaBLAM under varying luciferin concentrations to those expressing GCaMP8s. There was no significant difference in the proportion of responsive neurons between GCaMP8s and CaBLAM, regardless of Fz concentration, in response to 1 ms electrical field stimulation (**left, Fig. 5D**, Kruskal Wallis test $\chi^2(2) = 5.02,\ \mathrm{P} = 0.081)$. This indicates that CaBLAM's bioluminescent signal can reliably report single field stimulations, comparable to the state-of-the-art fluorescent indicator GCaMP8s. In contrast, delivery of 40 electrical field stimulations revealed a significant difference in the proportion of responsive neurons between CaBLAM-expressing neurons and those expressing GCaMP8s, with CaBLAM showing decreased responsivity at lower concentrations of Fz (**right, Fig. 5D**, Kruskal Wallis test: $\chi^2(2) = 24.3,\ P = 5.23 \times 10^{-6}$). Pairwise comparisons indicated that CaBLAM expressing neurons in the presence of 1:1x Fz had a significantly higher proportion of responsive neurons compared to 1:2x Fz ($P = 4.79 \times 10^{-4}$). The mean response rate was 97.9% for GCaMP8s, 84.2% for CaBLAM at 1:1x Fz, and 56.3% for CaBLAM at 1:2x Fz, suggesting that the 1:1x Fz concentration yields observed evoked responses similar to those of GCaMP8s ($P = 0.109$). The lack of statistically significant difference overserved between CaBLAM at 1:1x Fz and GCaMP8s ($P = 0.109$) is most likely due to variability and low sample size of the GCaMP8s cohort. Regardless, while nearly all GCaMP8s expressing neurons were responsive, CaBLAM expressing neurons also demonstrated robust responsiveness that is enhanced at higher Fz concentration.

Comparison of CaBLAM and GCaMP6s *in vivo*

We imaged genetically defined cortical layer 1 interneurons in NDNF-Cre mice to characterize and compare the performance of CaBLAM and GCaMP6s indicators *in vivo* (**Fig. 6**). After selective viral expression and surgical preparation, we performed *in vivo* imaging either under anesthesia without external illumination (for CaBLAM) or in an awake, head-fixed animal with epifluorescent illumination (for GCaMP6s). These approaches allowed us to directly assess bioluminescent and fluorescent calcium signals evoked by tactile stimulation of the mystacial vibrissae. All animals showed detectable single cells in the imaging field of view, and most of these cells exhibited clear calcium events (**Fig 6E** and **F**). The two CaBLAM animals exhibited 30 and 8 ROIs (27 and 6 ROIs with statistically detectable events, respectively), and the GCaMP6s animal showed 27 ROIs, all of which had detectable calcium events. The rate of calcium events in the CaBLAM mice was lower than that of the GCaMP mouse (CaBLAM: medians = 0.008 and 0.010 Hz, IQR = 0.008 Hz and 0.01 Hz; GCaMP6s: median = 0.029 Hz, IQR = 0.01 Hz), which may be attributable in part to the anesthetized versus awake states of the animals but also may be due to the lower absolute signal intensity of CaBLAM. Calcium events in the CaBLAM animals were somewhat smaller than those in the GCaMP6s mouse (**Fig. 6I** CaBLAM: median = 0.48 and 0.33 ΔL/L, IQR = 0.55 and 0.42; GCaMP6s: median = 0.72, IQR = 1.03). When normalized to their peaks, the median event waveforms of the 3 animals are very similar in shape (**Fig. 6G**). Stimulus-evoked activity in the same data revealed sparse, late peaking activity across the animals, in line with a previous report of stimulus responses in these interneurons[36]. **Fig. 6I** shows an example CaBLAM ROI tactile response to 49 stimulus presentations, and **Fig. 6J** shows a corresponding example GCaMP6s ROI response to 40 stimulus presentations. These results provide proof of concept evidence that CaBLAM can be employed *in vivo* to detect physiologically relevant neural calcium activity at the single cell level.

We conclude that CaBLAM's properties as a BL GECI, particularly its high absolute contrast and its practical contrast within a physiologically relevant range of Ca^{2+} concentrations, are uniquely well suited to single-cell resolution imaging and other advanced downstream applications.

Discussion

While the first known GECIs were naturally-occurring bioluminescent proteins[10–12], fluorescent small molecule dyes and FP-based GECIs are the currently most popular tools for reporting Ca^{2+} activity in living systems. The primary limitation of bioluminescent probes relative to fluorescent probes has been their lower rate of photons emitted per indicator molecule at saturating Ca^{2+} concentrations. This peak emission intensity can be increased linearly over several orders of magnitude for fluorescent probes simply by increasing the intensity of the excitation light that is delivered to the sample, but is limited by enzyme kinetics in bioluminescent probes. At the same time, all fluorescent probes undergo photobleaching during imaging which worsens as excitation intensity increases. In intact tissues, autofluorescence from endogenous molecules limits detection of weak fluorescent signals, supplying excitation photons becomes a major technical challenge, and confounding effects such as heating from intense excitation are of major concern. Bioluminescent probes hold promise for circumventing these and other limitations of fluorescence, especially when used in deeper tissues.

While the signal-to-noise ratio advantage afforded by elimination of autofluorescent background partially compensates for the low light output of luciferases in imaging, required exposure times have historically been in the tens of seconds, far from what is necessary to observe meaningful Ca^{2+} dynamics and other fast cellular processess. Imaging changes in intracellular Ca^{2+} at high speeds is possible only when the contrast of an indicator is well above the electronic noise in the camera. BL GECIs derived from GeNL imaged at up to 60 Hz in iPS-derived cardiomyocytes[17], which display very large changes in cytosolic Ca^{2+} concentration relative to most cells, displayed a dynamic range of less than 2-fold despite *in vitro* characterization suggesting much higher contrast. We observe that in HeLa cells displaying smaller swings in Ca^{2+} concentration when responding to histamine stimulation, the high baseline luminescence of the GeNL(Ca^{2+}) sensor family limits the achievable dynamic range (**Fig. 2**). In neurons, CaBLAM reliably reports responses to single action potential stimulation like GCaMP8s when imaged at 10Hz, and can be imaged indefinitely without photobleaching or phototoxicity. Future improvements to CaBLAM's BL brightness are expected to bring it closer to parity with fluorescent GECIs and allow even faster imaging with lower noise.

Biochemical indicators using BL as their output modality hold the promise of enabling less invasive and deeper imaging of these events than is possible with fluorescent sensors. CaBLAM will facilitate this type of imaging because of its low baseline signal, preventing a washout of true signal from scattered out-of-focus emission that is common for both fluorescent and BL GECIs in thick tissues. We also plan to use CaBLAM to drive optogenetic elements such as channelrhodopsins and light-sensitive transcription factors, making them response to changes in intracellular Ca^{2+}, building on previous work fusing bioluminescence and optogenetics[37–43].

Here, we demonstrate that structure-guided engineering and directed evolution can generate large improvements in luciferase solubility and toxicity while maintaining high catalytic activity, and that highly active and soluble luciferases can be used to engineer biochemical indicators with large signal changes in cells. The scaffold and design principles we have identified will be useful in the design and optimization of BL sensors for other biochemical activities as well[44]. In the future, development of improved red-emitting FRET acceptors (such as optimized long Stokes-shift fluorescent proteins) and/or engineering of high-activity, red-emitting substrates for SSLuc/CaBLAM will further enhance the deep-tissue imaging potential of these probes. Continued efforts will also focus on further improving the light production rate of this and other classes of luciferase. Looking forward, if K_m values are maintained at ~10μM, a diffusion-limited luciferase (i.e., $k_{cat}/K_m = 10^8\text{-}10^9\ M^{-1}s^{-1}$) should be capable of generating $10^3\text{-}10^4$ photons per second per molecule, which leads us to hope that there is ample room left for future improvements to these enzymes. Given our current observations, efforts to increase the delivery rate of engineered luciferins to the cytoplasm of target cells will be central to realizing the full potential of bioluminescent imaging probes.

Materials and Methods

General molecular biology.

E. coli strain NEB 10-beta (New England Biolabs) was used for all cloning, library screening, and recombinant protein expression. PCRs were performed using Phusion DNA polymerase (New England Biolabs) and the supplied 'GC buffer' under manufacturer-recommended conditions. DNA oligonucleotide primers were purchased from IDT. Restriction enzymes were purchased from New England Biolabs and restriction digests followed the manufacturer's protocols. All plasmids were constructed using Gibson assembly[45] of PCR or restriction digest derived linear DNA fragments as previously described[23,46]. Unless otherwise noted below, chemicals were purchased from Sigma-Aldrich.

Construction of *E. coli* expression plasmids and libraries.

All *E. coli* expression plasmids were constructed using the pNCST backbone as previously described[23,46]. A linear DNA fragment of the pNCST vector was generated by PCR (primers, **Supp. Data File 2**). Designed luciferase and novel GECI coding sequences were initially prepared as synthetic genes (IDT), as were many designed variants during directed evolution in cases where site-directed mutagenesis would be impractical. Mammalian expression plasmids encoding GeNL(Ca^{2+})_480[17] (plasmid #85205) and CaMBI[18] (plasmid #124094) were obtained from AddGene and amplified by PCR (primers, **Supp. Data File 2**) for insertion into the pNCST expression vector. Error-prone mutagenesis was performed using the GeneMorph II kit (Agilent Technologies) as previously described[23] with a target mutation rate of ~5 base changes per kilobase of amplified product. Site-directed libraries were constructed by Gibson assembly of PCR fragments amplified to introduce mixed-base codons as previously described[23]. Selected clones from library screening were sequenced using standard Sanger sequencing (Eton Biosciences). Libraries were introduced to *E. coli* via electroporation with plating at densities between 10^3 and 10^5 colonies per 10cm petri dish of LB/Agar supplemented with 100µg/mL carbenicillin (Fisher BioReagents) and incubated overnight at 37C. All plasmid sequences are provided in the **Supplementary Sequences** text file.

Luciferin substrates and library screening.

Native coelenterazine (CTZ) was purchased from NanoLight. Furimazine (Fz) stock solution was purchased from Promega as a component of the Nano-Glo® Luciferase Assay System (cat# N1110 or N1120). Because Promega does not disclose the Fz concentration in their stock solution, we hereafter describe Fz concentrations in terms of dilution ratio (typically a 1:500 or 1:1000 dilution of the Fz stock solution for imaging and 1:100 for *in vitro* assays). Error-prone mutagenesis and site-directed libraries of luciferases were screened by spraying a sterile solution of 50µM CTZ or 1:100 Fz in 50mM Tris-HCl pH 7.5 onto individual plates using a small atomizer. For 'manual' screening, the entire screening process was performed in complete darkness or very dim far-red LED light, with care taken to dark-adapt vision prior to starting. Sprayed plates were examined by eye and the brightest colonies were immediately marked. For image-based screening, plates were placed immediately into a light-tight chamber and imaged with a PRIME 95b sCMOS camera (Photometrics), followed by identification of the brightest colonies using ImageJ and manual marking on the plates. Marked colonies were grown individually in 5ml 2xYT medium supplemented with 100µg/mL carbenicillin with shaking at 250 rpm at 37C overnight.

Protein Expression, Purification, and *in vitro* experiments.

The pNCST plasmid is useful for protein library screening and expression because it does not require an inducer in most strains of *E. coli*. For characterization of selected luciferase and GECI clones, 1ml of each overnight liquid culture was pelleted by centrifugation and the supernatant was discarded. The bacteria were then resuspended once in ultrapure water to remove residual culture medium and pelleted again by centrifugation, discarding the supernatant. The washed pellet was then resuspended in 400µL B-PER (Thermo) reagent and incubated at room temperature for 20 minutes with gentle rocking to extract soluble proteins, followed by a final centrifugation to pellet insoluble components and yield a clear lysate. Clarified B-PER lysates were used directly for characterization experiments in most cases, since we observed rapid degradation of some proteins when subjected to additional purification procedures. In all cases, proteins prepared as clarified B-PER lysates were assayed within 6 hours of extraction.

For experiments using purified recombinant protein, B-PER lysates were bound to equilibrated cobalt beads as previously described[23,46], washed, and eluted in 50mM Tris-HCl pH 7.5, 150mM NaCl, 500mM imidazole, then buffer-exchanged into 50mM Tris-HCl pH 7.5, 150mM NaCl using Zeba desalting columns (Pierce). Purified proteins were stored at 4C.

For brightness comparisons *in vitro*, B-PER lysates of mNG-fused luciferase clones were diluted in 50mM Tris-HCL pH 7.5, 150mM NaCl to a peak mNG absorbance value <0.05 and 200µL samples were loaded into a clear-bottom black 96 well plate (Corning) along with B-PER lysates from one or more controls (e.g., GeNL). Fluorescence emission spectra were recorded for each sample with excitation at 480nm (5nm bandwidth) using a Tecan M1000Pro Infinite multimode plate reader. To normalize enzyme concentrations based on the fluorescence, a dilution factor was calculated for each well based on the peak fluorescence emission. Samples were then diluted into new wells to a total volume of 50-100µL and were measured again to verify that fluorescence intensities varied by ≤ 5% over all wells. The plate was then transferred to a ClarioStar multimode plate reader (BMG) to measure luminescence kinetics. Luciferin solutions at 50µM (CTZ) or 1:100 (Fz) were prepared in the same Tris buffer as described above and injected in volumes of 100-150µL individually into wells with concurrent measurement of luminescence intensity for a total measurement time of 50s per well. These sample and injection volumes were chosen to reduce variability in measurements due to uneven mixing, which can occur if the injection volume is smaller than the sample volume. Peak and steady-state intensities were then normalized by dividing by the previously measured fluorescence of each well to account for remaining small variations in concentration between wells, and these normalized values were used for brightness comparisons between clones.

For Ca^{2+} titrations *in vitro*, B-PER lysates of mNG-fused GECIs were diluted ~100-fold in 30mM MOPS pH 7.2, 100mM KCl, 10mM $MgCl_2$ and then dispensed into 3 rows (36 wells) of a 96-well plate, 5µL per well. EGTA-buffered Ca^{2+} solutions with free Ca^{2+} concentrations of 2nM, 20nM, 100nM, 200nM, 300nM, 400nM, 600nM, 800nM, 1µM, 1.5µM, 2µM, and 10µM were then prepared from commercial stock solutions (Invitrogen

cat#C3008MP), also in 30mM MOPS pH 7.2, 100mM KCl, supplemented with $MgCl_2$ to a final concentration of 10mM. The presence of Mg2+ is not expected to alter free Ca^{2+} concentrations in EGTA-based buffers and provides a more physiologically relevant environment for this assay. 100µL of Ca^{2+} buffer solution was added to each well containing sample to produce three identical rows of the same concentration series. A solution of 1:100 Fz in the same Mg^{2+}-containing MOPS buffer was prepared and injected in volumes of 100µL individually into wells with concurrent measurement of luminescence intensity for a total time of 20s per well. The maximum, steady-state, and area-under-the-curve (AUC) luminescence values were calculated for each well and used to plot the Ca^{2+} binding curve for each GECI. Curve fitting to a sigmoid function was performed using the Solver add-in in Excel to determine the K_D, Hill coefficient, and contrast for each GECI tested.

Construction of mammalian expression plasmids.

Mammalian expression constructs were mainly generated by Gibson assembly of PCR-amplified coding sequences (primers, **Supp. Data File 2**) into restriction-digested pC1 (CMV promoter, modified from pEGFP-C1, Clontech) or pCAG (CMV enhancer fused to chicken beta-actin promoter) vector fragments. When vector fragment preparation by restriction digest was impractical, we PCR-amplified vector fragments instead (primers, **Supp. Data File 2**). We observed qualitatively less variable and longer-lasting expression using the pCAG vector in most cases. Both vectors were suitable for all constructs tested. Mammalian expression plasmids encoding GeNL(Ca^{2+})_480[17] (plasmid #85205) and CaMBI[18] (plasmid #124094) were obtained from AddGene. The plasmid pCAG_EGFP_GPI (plasmid #32601) was obtained from AddGene and digested with *Sac*I and *Xho*I to generate a vector fragment for insertion of GeNL and GeNL_SS for GPI-anchored extracellular display. All plasmid sequences are provided in the **Supplementary Sequences** text file.

Cell line culture, Transfection, and Imaging.

HeLa and U2OS cell lines were purchased from ATCC. Cells were maintained under standard culture conditions with incubation at 37C and 5% CO2. Growth medium for HeLa cells was high-glucose DMEM (Gibco) supplemented with 10% fetal bovine serum (FBS) (Gibco), and for U2OS was McCoy's 5a (Gibco) with 10% FBS. For transfection and imaging, cells were plated at a density of 1-2x10^5 cells/ml on coverslip-bottom 35mm dishes (Mattek) or 13mm round coverslips (BioscienceTools) placed in 6-well culture plates and incubated overnight. The following day, cells were transfected using polyethyleneimine (PEI) as previously described[46]. Cells were imaged 24-48h post-transfection.

Prior to imaging non-sensor luciferase constructs and fusions, cells were gently rinsed with fresh medium, leaving 500µL of medium in each dish for Mattek dishes. For cells plated on coverslips, slips were transferred to a low-profile coverslip chamber (BioscienceTools) with a silicone gasket and overlaid with 500µL medium. In either case, cells were transferred to the stage top environmental chamber and allowed to equilibrate for at least 5 minutes prior to imaging.

Image acquisition was performed in a stage-top environmental enclosure (37℃, 5% CO2; Okolab) on a Nikon Ti-E microscope and an Andor iXon Ultra 888 EMCCD camera. Cells expressing bioluminescent constructs

were imaged with a Plan Apo λ 20x Ph2 DM 0.75NA objective (Nikon). For reference fluorescent images in constructs containing mNeonGreen, green fluorescence was excited with a Spectra X LED source (Lumencor) using the 475/28nm channel and a FF495-Di03 dichroic (Semrock) and emission was selected with a FF01-520/35 filter (Semrock). The camera was set to 30MHz EM gain mode with an EM gain setting of 3 for fluorescence acquisition. For bioluminescent signal recording, the illumination source was turned off and emission was collected either with no filter to maximize light collection efficiency or with the FF01-520/35 filter to minimize background light leakage. The camera was set to 30MHz EM gain mode with an EM gain of 300 and exposure times between 50 and 500ms for bioluminescence time series and between 500ms and 10s for single for most datasets.

For Ca^{2+} indicator time series imaging, cells were only plated in Mattek dishes and were not rinsed, a handling method we found prevented induction of extraneous Ca^{2+} signals in the cytosol. Medium was carefully removed to leave 500µL volume remaining in each dish, and 500µL of medium from the dish was reserved and used to dilute the Fz substrate to eliminate small changes in ionic strength and osmolarity that can arise due to evaporation during culture. Baseline images were collected for at least 30s in the dark prior to luciferin addition. Fz diluted in culture medium was added to a final concentration of ~10µM and the BL signal was recorded for 60s. For determination of the maximal contrast in cells, 50µL of concentrated ionomycin was then injected to give a final concentration of 20µM and images were recorded for an additional 60-120s. The concentration of Ca^{2+} in the culture medium was ~1mM (but likely buffered to some degree by other medium components) and therefore expected to produce a "maximal" physiological Ca^{2+} concentration in the cytosol in the presence of ionomycin. For imaging induced Ca^{2+} oscillations, 50µL of concentrated L-histamine was injected to give a final concentration of 50µM and images were recorded for an additional 10-20min.

Primary Rat Cortical Neuron Culture, Transfection, and Ca^{2+} Imaging.

Animal procedures were approved by the Institutional Animal Care and Use Committee of UC San Diego. Cortices were dissected out from P2 Sprague-Dawley rats and neurons were dissociated using papain as previously reported[47]. Transfection of neuronal cells with pCAG-CaBLAM and pCAG-GeNL(Ca^{2+})_480 was done by electroporation using an Amaxa Nucleofection Device (Lonza) at day-in-vitro 0 (DIV0). Neurons were cultured on poly-D-lysine (PDL) coated 35mm coverslip-bottom dishes (Mattek) in Neurobasal A medium (Life Technologies) supplemented with 1X B27 Supplements (Life Technologies), 2 mM GlutaMAX (Life Technologies), 20 U/mL penicillin, and 50mg/mL streptomycin (Life Technologies) for 2-3 weeks prior to imaging, refreshing half medium every 2-3 days.

For Ca^{2+} imaging with KCl-mediated depolarization, Mattek dishes were treated similarly to cell lines, with removal of all but 500µL medium, equilibration in the stage-top incubation chamber on the microscope, and imaging following the same basic protocol as described above for ionomycin and L-histamine experiments. Dark images were recorded for ~30s, followed by injection of Fz diluted in 1000µL medium at a final concentration of 50µM and incubation for 60s with continuous imaging. Finally, 500µL of 120mM KCl diluted in medium was

rapidly injected to give a final concentration of 30mM KCl, expected to rapidly depolarize all neurons leading to Ca^{2+} influx.

Primary Rat Hippocampal Neuron Culture, AAV Transduction, and Ca^{2+} imaging.

Primary E18 rat hippocampal neurons were prepared from tissue shipped from BrainBits (Transnetyx) following the vendor's protocol. Neurons were seeded on PDL-coated 18 mm glass coverslips (Neuvitro) in 12-well tissue culture plates (1 x 10^5 neurons per well) and grown in Gibco Neurobasal Media supplemented with 2% B27, 0.1% gentamycin and 1% GlutaMAX (all from Invitrogen). The next day, day-in-vitro 1 (DIV1), neurons were transduced with AAV9-Syn (5 x 10^9 gc per well) encoding jGCaMP8s (AddGene 162374) or CaBLAM (in house prep). AAV9-Syn-CaBLAM was generated by triple lipofection of HEK293-FT cells and harvesting viral particles as previously described[48]. Neurons were imaged between DIV 20 – 30.

For Ca^{2+} imaging with electrical stimulation, cover slips were washed three times and imaged in artificial cerebrospinal fluid, containing (in mM): 121 NaCl, 1.25 NaH_2PO_4, 26 $NaHCO_3$, 2.8 KCl, 15 d(+)-glucose, 2 $CaCl_2$, 2 $MgCl_2$ (maintained at ~37 °C, pH 7.3-7.4, continuously bubbled with 95% O_2/5% CO_2 vol/vol). All imaging was conducted in the RC-49MFSH heated perfusion chamber where the temperature was continuously monitored (Warner Instruments). Only cultures where neurons were evenly distributed across the entire coverslip. In addition, only coverslips with minimal neuronal clumping/astrocytic growth were included for Ca^{2+} imaging. A Teensy 3.2 microcontroller was utilized to synchronize the camera frame number with electrical stimulation using BNC cables connected to EMCCD camera and the SIU-102 stimulation isolation unit (Waner Instruments). Custom written scripts were developed in order to generate analog signals for precise control current stimulation as previously described[49]. Briefly, current field stimulation with a 1ms pulse width at 40mA and 83Hz was utilized. The length of time for each stimulation period was varied (12, 36, 60, 120, 240, 960, 1920ms) in order to achieve the corresponding number of action potentials (1, 3, 5, 10, 20, 80, 160 action potentials).

For fluorescent and bioluminescent Ca^{2+} imaging, a 20x objective lens (0.75 NA) and iXon Ultra 888 EMCCD (Andor Technology) camera were used. Furimazine (Fz) (Promega, N1120) was diluted in bubbled ACSF at concentrations of 1:1000 (0.5x) or 1:500 (1x), both of which provided sufficient bioluminescent signal for imaging at 10Hz. Image acquisition parameters were as follows: 0.09s exposure time, 4.33 us vertical pixel shift, normal vertical clock voltage amplitude, 10MHz at 16-bit horizonal readout rate, 1x pre-amplifier gain, 2x2 binning. The EM Gain was set to 300 for bioluminescent image acquisition and it was not enabled during fluorescent imaging. ACSF was continuously perfused in the heated chamber prior to imaging and during bright field and fluorescence imaging to determine a field of view before beginning bioluminescent Ca^{2+} imaging. During bioluminescent Ca^{2+} imaging, fresh ACSF was utilized to dilute the Fz and kept at 37C in a water bath. Bioluminescent imaging included a 60s initial period of ACSF perfusion without Fz followed with ACSF/Fz at the designated concentration for the remainder of the imaging session. Fz concentration in the imaging chamber typically reached equilibrium within 60s after initiating ACSF/Fz perfusion, as judged by baseline bioluminescent signal in the neuron cell bodies.

Image processing and data analysis

All image processing was performed using ImageJ. It is important to note that processing of bioluminescence imaging data requires compensation for the average dark pixel offset arising from the detector's dark current characteristics and by small light leaks in the optical path. For each acquisition setting, dark time series were acquired under identical conditions but without illumination or addition of luciferin substrates. Dark time series with at least 60 frames were used to generate single-frame 'dark' images for each acquisition setting, containing the median value for each pixel over the time series. For single bioluminescence images of fusion proteins, the appropriate dark image was subtracted from the raw image. For time series, the appropriate dark image was subtracted from each frame of the time series. These dark-subtracted time series were summed using the 'Z project' function in ImageJ to create low-noise images for generation of regions of interest (ROIs) for analysis. Additional settings used for image display (e.g., thresholding, output scaling, lookup tables, etc.) are described for individual images in their corresponding figure legends.

To extract data from time series for downstream analysis, ROIs corresponding to individual whole cells were identified from summed time series images using the Cellpose[50] 'cyto' model followed by manual curation. An additional 'background' ROI was drawn manually for each time series in an area devoid of cells. Mean intensities were then measured for each ROI at each time point from the dark-subtracted time series and data transferred to Excel for subsequent steps. The 'background' ROI value was subtracted from each cell ROI at each time point to account for any variable background signal arising from changes in light leakage (for example, when the injection port is uncovered) as well as any bioluminescence generated by extracellular luciferase/GECI molecules that escape from damaged or dead/lysed cells. Note that in cases where cells can be rinsed, the extracellular bioluminescence signal is typically negligible, but baseline shifts from changes in light leakage are inevitable, in our experience, making this step critical for accurate quantitation. For each ROI (whole cell) in a time series, we additionally calculate the mean dark value during the first 30s prior to Fz injection and subtract this value from all time points to bring the dark baseline as close to zero as possible, compensating for any remaining offset in the data not captured by previous processing steps.

For Ca^{2+}indicators, the baseline luminescence emission intensity was determined for each cell by taking the average value of time points in the steady-state phase after initial Fz injection but before ionomycin or L-histamine injection, typically observed between 30 and 40s after Fz injection (following a small transient cytosolic [Ca^{2+}] increase) in most cells. The indicator signal at each time point was then calculated as the change in luminescence relative to the baseline luminescence ($\Delta L/L_0$) for each cell.

***In vivo* Ca^{2+} imaging**

Animals. Three NDNF-Cre mice (1 female/2 male; JAX stock #030757) were used for *in vivo* imaging to selectively express CaBLAM or GCaMP6s in neuron-derived neurotrophic factor expressing cortical layer 1 interneurons[51]. Mice were housed in a vivarium on a reversed light-dark cycle and had free access to food and water. All procedures were conducted in accordance with the guidelines of the National Institute of Health and with approval of the Animal Care and Use Committee of Brown University.

Surgical procedures. Two mice were injected with an AAV vector encoding a floxed version of the CaBLAM sensor (AAV9-ef1a-DIO-CaBLAM) and the third mouse was injected with a floxed version GCaMP6s (AAV2/1-CAG-FLEX-GCAMP6s). Each animal was anesthetized (1-2% isoflurane), fitted with a steel headpost, and injected with viral constructs in a 3 mm craniotomy centered over left SI barrel cortex (-1.25 A/P, 3.5 M/L relative to bregma) made with a dental drill. Mice received 4 injections of the constructs at locations equidistantly spaced around the central SI point at depths of 200 µm. Each injection was 200 nl in volume and delivered at a rate of 50 nl/min. Viral injections were performed through a glass pipette fitted in a motorized injector (Stoelting Quintessential Stereotaxic Injector, QSI). A glass window was then fitted over the open craniotomy and cemented in place with dental cement (C & B Metabond).

Image acquisition. Images were acquired using an Andor Ixon Ultra 888 EMCCD camera and a 16x 0.8NA objective (Nikon CFI75 using Andor Solis data acquisition software (Andor Solis 64 bit, v4.32). Imaging data of the CaBLAM mice were acquired under no illumination in a light shielded enclosure (512 x 512 pixels after 2x2 binning, 1.625 µm2/pixel) at a frame rate of 5 Hz and an electron multiplication gain of 300. The GCaMP6s mouse was imaged (1024x1024, 0.8125 µm2/pixel) under epi-illumination from a X-Cite 120Q mercury vapor lamp (Excelitas Technologies) using an EGFP filter cube (Chroma 49002, excitation filter: ET470/40x, dichroic: T495lpxr, emission filter: ET525/50m) at a frame rate of 10 Hz and an electron multiplication gain of 0.

Experimental procedures. Experiments were conducted a minimum of 5 weeks after surgery. On the day of the experiment, the CaBLAM animals were anesthetized (1-2% isoflurane) and a dental drill was used to remove the cement holding the cranial window in place. The window was then lifted off to expose the open craniotomy. For the duration of the experiment the craniotomy was kept covered in saline. The animal remained anesthetized for the entirety of the experiment. Water soluble h-coelenterazine (Nanolight, CAT#3011) was dissolved in sterile saline (4.55 µg/µl). The solution was loaded into a 100 µl glass syringe (Hamilton #80601) fitted with a ~1 cm length of 18 gauge plastic tubing. The Hamilton syringe and tubing was placed in a motorized injector (Stoelting Quintessential Stereotaxic Injector, QSI). The tip of the plastic tubing was lowered into the pool of saline and the Luciferin was delivered by infusing 50 µl of the solution into the saline over the open craniotomy at a rate of 200 µl/min after which data were acquired for ~1 hour. The GCaMP6s mouse was awake, head fixed and on a running wheel for a ~5-minute imaging session. For all animals, throughout data collection, a tactile stimulus was delivered to the right mystacial vibrissa pad using a piezo bender (Noliac). Tactile stimuli consisted of asymmetric sinusoidal deflections (10 ms rise and 24 ms fall time, 5 repetitions, 125 ms total stimulus length) delivered at random intervals between 7 and 15 seconds. During the ~1-hour CaBLAM imaging sessions a variety of imaging parameters were tested. While bioluminescence was observable at imaging rates as high as 10 Hz and no pixel binning, a ~5-minute timeseries at the parameters listed above yielded the qualitatively best images. As such we used these shorter segments to compare CaBLAM with the ~5-minute imaging session of the GCaMP6s animal. We recommend use of furimazine or its derivatives for *in vivo* imaging of CaBLAM to generate brighter signals that will allow for faster imaging.

Data analysis. Offline analyses of the imaging data were performed in Matlab R2023a (Mathworks). Dark images (median 50 frames) were subtracted from each image time series. Images were median binned to yield an image size of 256 x 256 pixels and the GCaMP6s data was median down sampled from 10 Hz to 5 Hz. The Matlab toolbox MIN1PIPE[52] was used to denoise the images and perform background subtraction. ROIs were then drawn by hand using the mean projection image and timeseries were extracted for each ROI. The resultant time series were smoothed using a 1s moving average window. Calcium events were detected by finding peaks in the data that exceed a threshold of 1.5 times the inter-quartile range above the median with the further criterion that the peak had to exceed this threshold for 5 consecutive data points (1s). Time windows of -10 to 10 seconds around the peaks were extracted from the timeseries and ΔF/F or ΔL/L was computed by using a baseline value of the mean of the data from -10 to -2 seconds prior to peak onset, the event windows were then cropped down to -6 to 6 seconds for presentation purposes. In order to analyze stimulus evoked activity we extracted -3 to 10 second windows centered on stimulus onset for each stimulus presentation and all ROIs. The waveforms were then baselined to the mean of the period -3 to 0 seconds prior to stimulus onset to yield ΔF/F or ΔL/L.

Acknowledgments

We wish to thank several individuals who supported this project as allies: Dr. Stephen Adams for many years of insightful discussions about sensors, calcium buffers, and other subjects; Dr. Pauline Wales for her invaluable help with camera and objective selection and optimization; Dr. Justine Allen for critical organizational and administrative support; and Dr. Leona Flores, Dr. Michael Oberholzer, and Dr. David Schoppik for invaluable scientific discussions and moral support through very challenging times. We would also like to thank all members of our Bioluminescence Hub (http://www.bioluminescencehub.org/) laboratories for their feedback, discussions, and thoughtful comments throughout the progression of this work.

Competing interests

The authors declare no competing or financial interests.

Author contributions

Conceptualization, GGL, ELC, DL, CIM, UH, and NCS; Validation, GGL, ELC, JM, SV, DC, DL, CIM, UH, NCS; Formal Analysis, GGL, ELC, JM, NCS; Investigation, DB, JH, SL, DKN, BS, MOT, SV, DC, RO, DH, ABB, ATZ, AH, NCS; Data Curation, GGL, ELC, JM, NCS; Writing—Original Draft, GGL, ELC, NCS; Writing—Review & Editing, GGL, ELC, BS, DL, CIM, UH, NCS; Visualization, GGL, ELC, JM, NCS; Supervision, DL, CIM, UH, NCS; Project Administration, UH, NCS; Funding Acquisition, DL, CIM, UH, NCS

Data and reagent availability

Raw and processed data from experiments performed in this study will be made available to other researchers upon request to NCS. Bacterial and mammalian expression plasmids encoding SSLuc, GeNL_SS, and CaBLAM will be deposited for distribution by AddGene (pending); prior to availability from AddGene, plasmids will be shared with non-profit researchers upon request to NCS.

Funding

This work was supported by National Institutes of Health grants R21EY030716, R21MH101525, R01GM121944, and U01NS099709, and National Science Foundation grants CBET-1464686 and DBI-1707352.

Tables

Table 1. Properties of selected intensiometric genetically encoded Ca^{2+} indicators

GECI Name	Type	K_D (nM)[a]	Hill coefficient[b]	Contrast[c]	ref.
GCaMP8s	FP	46	2.2	50	5
GCaMP8f	FP	334	2.1	79	5
NEMOf	FP	528	3.2	246	6
NEMOc	FP	557	3.8	422	6
CaMBI_110	luciferase	62 ± 16 (110)	1.2 (2.5)	4.3 (8)	18
GeNL(Ca^{2+})_480	luciferase	444 ± 150 (480)	3 (3)	4.1 (5)	17
CaBLAM	luciferase	464 ± 115	3	97	this work

[a]Binding constant for Ca^{2+} for FP-based GECIs as reported in the original publications; binding constant for Ca^{2+} as measured *in vitro* for CaMBI, GeNL(Ca^{2+})_480, and CaBLAM and (in parentheses) as reported in the original publications. Error margins represent 95% confidence interval for values measured in this work. [b]Hill coefficient (cooperativity) for FP-based GECIs as reported in the original publications; Hill coefficient for luciferase-based GECIs calculated from sigmoidal curve fit to Ca^{2+} titration series and (in parentheses) as reported in the original publications. [c]Contrast between Ca^{2+}-free and Ca^{2+}-saturated indicator *in vitro* for FP-based GECIs as reported in the original publications; contrast for luciferase-based GECIs measured in this work and (in parentheses) as reported in the original publications.

Figures

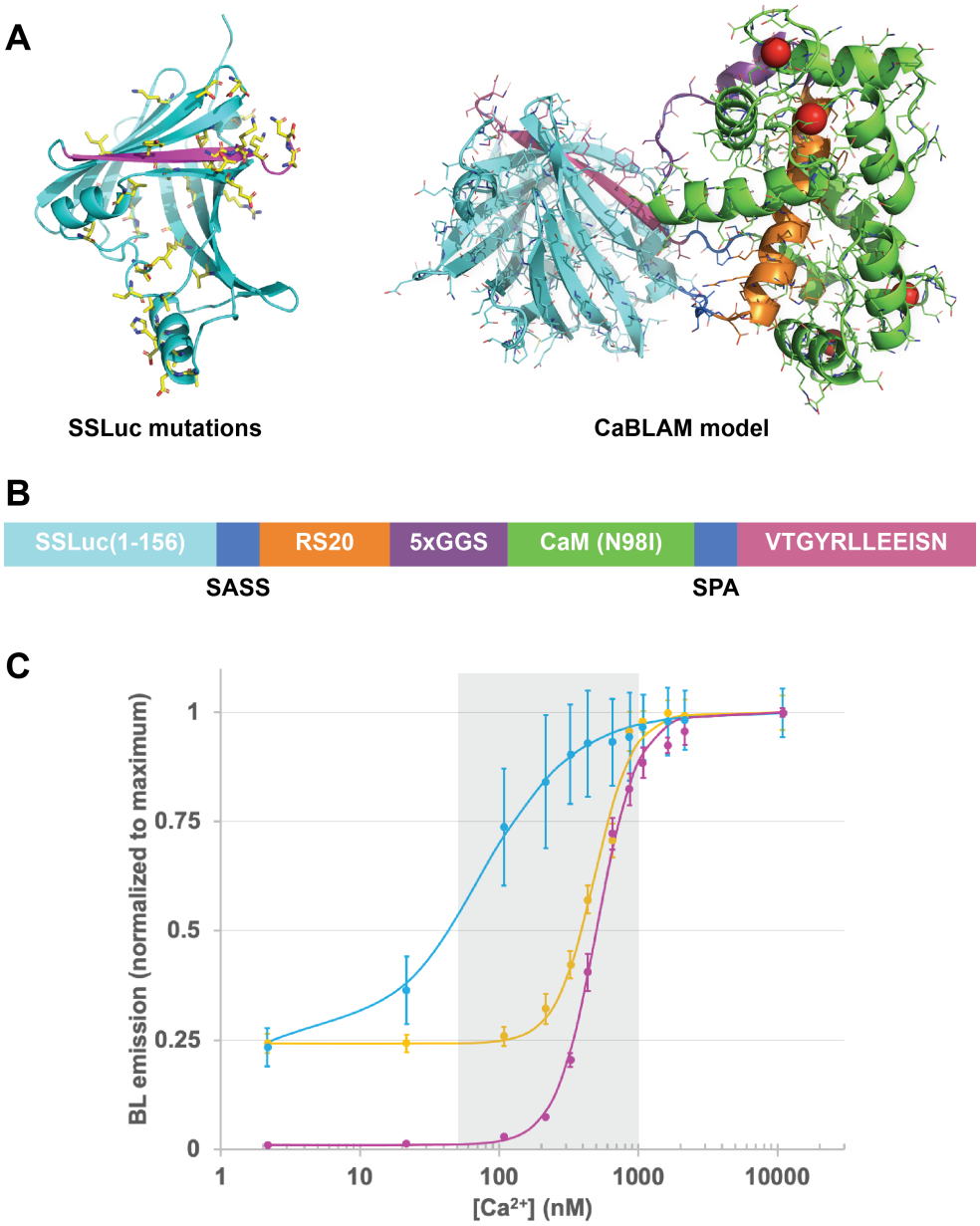

Figure 1. CaBLAM architecture and Ca^{2+} affinity. (A) Structure models of eKL9h and CaBLAM. Side chain positions with mutations relative to eKAZ are depicted as yellow sticks in the luciferase model. The C-terminal peptide is depicted in magenta on both structure models. (B) Architecture of CaBLAM (not to scale), with colors corresponding to the model structure backbone. (C) *In vitro* Ca2+ titration of CaBLAM (magenta) alongside GeNL(Ca2+)_480 and CaMBI_110. The physiologically relevant Ca2+ concentration range between 50nM and 1μM is shaded.

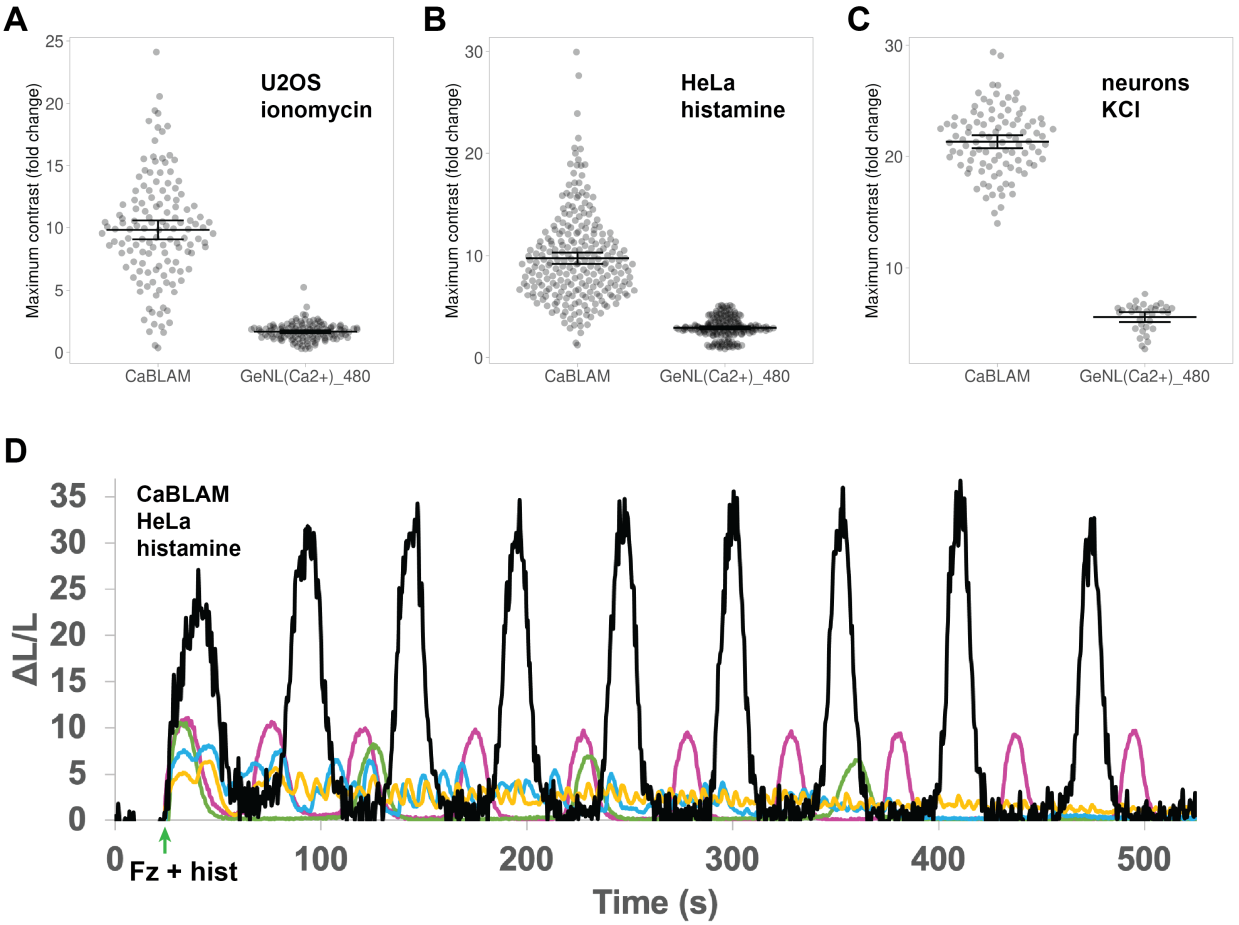

Figure 2. Characterization of CaBLAM in cultured cell lines and rat cortical neurons. CaBLAM and GeNL(Ca^{2+})_480 in (A) U2OS cells treated with ionomycin and 1mM external Ca^{2+}, (B) HeLa cells treated with L-histamine, and (C) rat cortical neurons depolarized with KCl. Data points represent contrast (fold change) between steady-state resting BL GECI signal and peak high-Ca^{2+} GECI signal after treatment. Each point corresponds to a single cell. Mean contrast is shown for each condition with error bars representing the 95%CI for each. (D) Representative CaBLAM signals in HeLa cells treated with L-histamine. Luciferin substrate (Fz) was injected along with L-histamine, indicated by the green arrow.

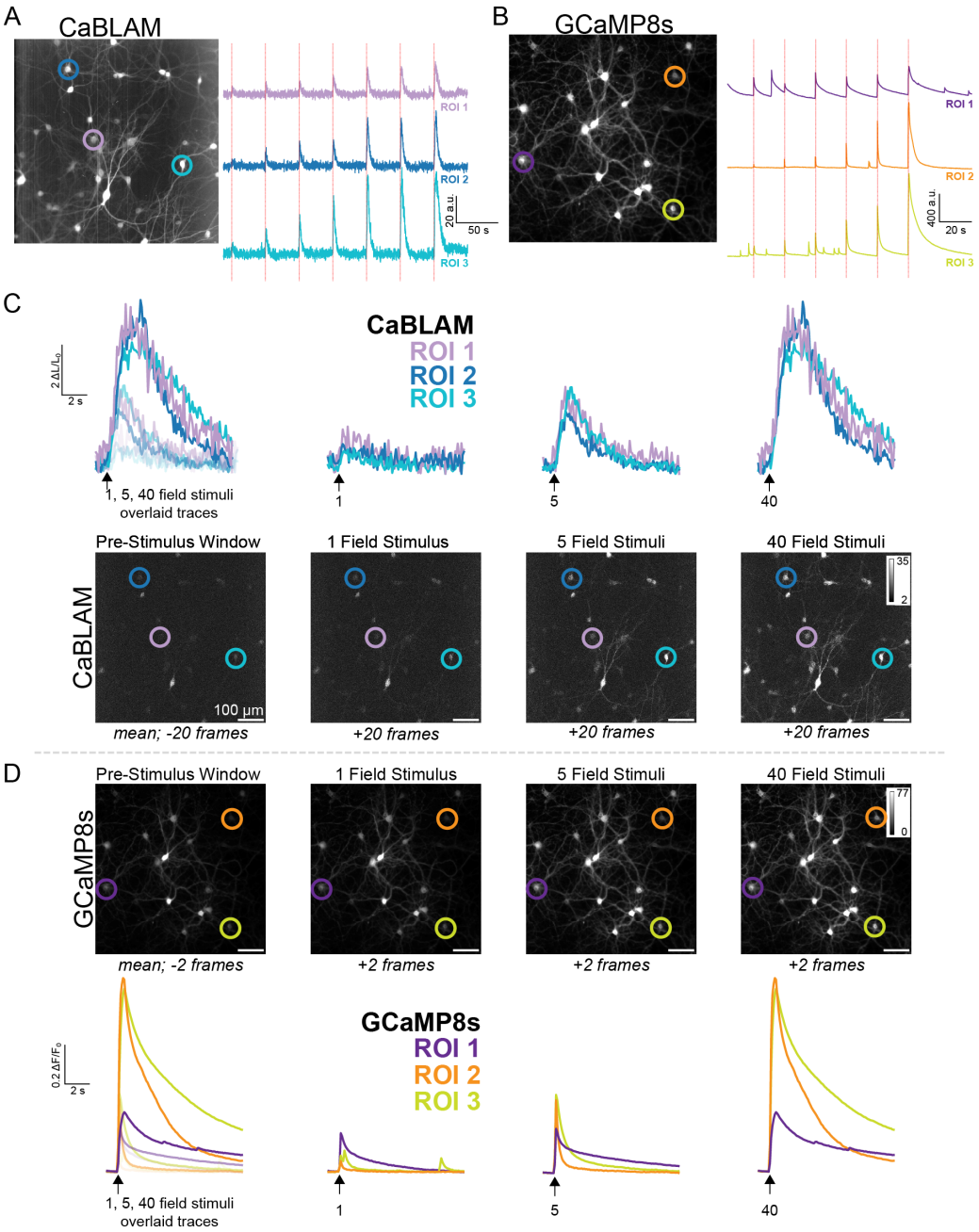

Figure 3. Overview of a typical calcium imaging session comparing electrical field evoked responses in CaBLAM and GCaMP8s expressing rat hippocampal neurons. (A) Representative CaBLAM bioluminescence imaging session. *left*: Mean z-stacked image of with regions of interest (ROIs) highlighted by colored circles (ROI 1 in light purple, ROI 2 in blue, and ROI 3 in teal). *right*: Bioluminescent calcium transients from ROIs 1-3 displaying responses evoked by multiple field stimuli (red dashed lines indicate field stimulation events). (B) Representative GCaMP8s fluorescence imaging session. *left*: Mean z-stacked image with individual ROIs highlighted by colored circles (ROI 1 in dark purple, ROI 2 in orange, ROI 3 in yellow). *right*: Fluorescence calcium transients from ROIs 1-3 displaying responses evoked by multiple field stimuli (red dashed lines indicate stimulation events). For both **a** and **b**, values are in arbitrary units (a.u.) (C) CaBLAM calcium responses to varied field stimuli. *top*: Individual bioluminescent Δ L/L calcium response traces from ROIs 1-3 for each field stimulus condition. *bottom*: Mean z-stacked frames (20 frames per condition) for pre-stimulus, 1 field stimulus, 5 field stimuli, and 40 field stimuli conditions, corresponding to data shown in the top panel. (D) GCaMP8s calcium

responses to varied field stimuli. *top*: Individual fluorescence ΔF/F calcium response traces from ROIs 1-3 for each stimulus condition. *bottom*: Mean z-stacked frames (2 frames per condition) for pre-stimulus, 1 field stimulus, 5 field stimuli, and 40 field stimuli conditions, corresponding to data shown in the top panel. For (C) and (D), arrows indicate field stimulus onset.

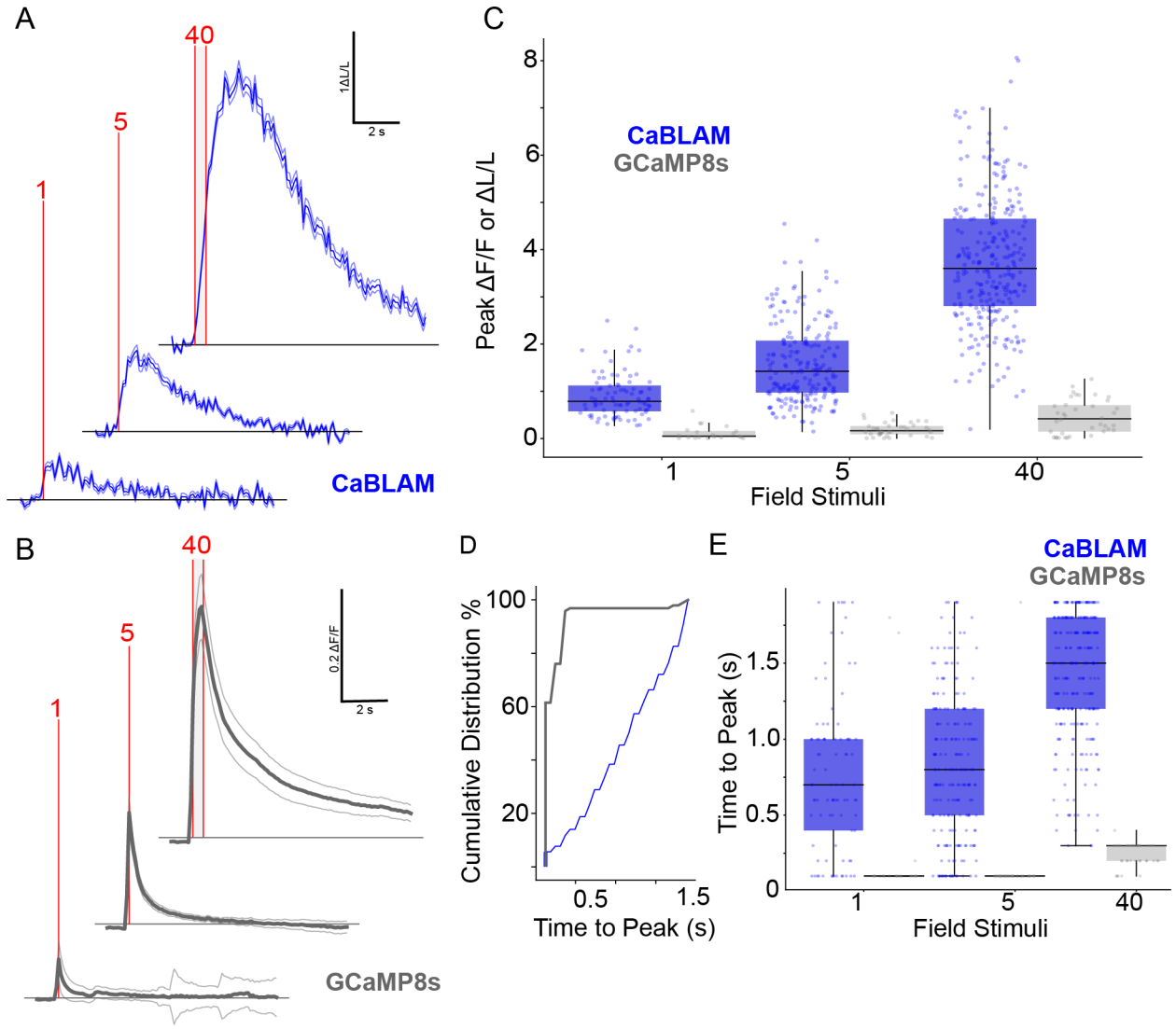

Figure 4. CaBLAM provides high-contrast reporting of stimulus-evoked neural activity in cultured neurons. (A) Bioluminescence ΔL/L time-locked traces of CaBLAM calcium responses to 1, 5, 40 pulses of 1ms field stimulations at 83 Hz (red dashed lines indicate field stimulation window). (B) Same as panel (A), but fluorescence ΔF/F time-locked traces for GCaMP8s. For panels (A) and (B), data are shown as mean ± s.e.m. (C) Peak stimulus evoked ΔF/F or ΔL/L across neurons across increasing field stimulations. (D) Cumulative distribution of time to peak ΔF/F or ΔL/L responses. (E) Time to peak ΔF/F or ΔL/L across neurons in response to increasing field stimulations. For panels (C) and (E), boxplots show the median, 25th and 75th percentiles (box edges), whiskers extending to the most extreme data points, and individual outliers plotted separately.

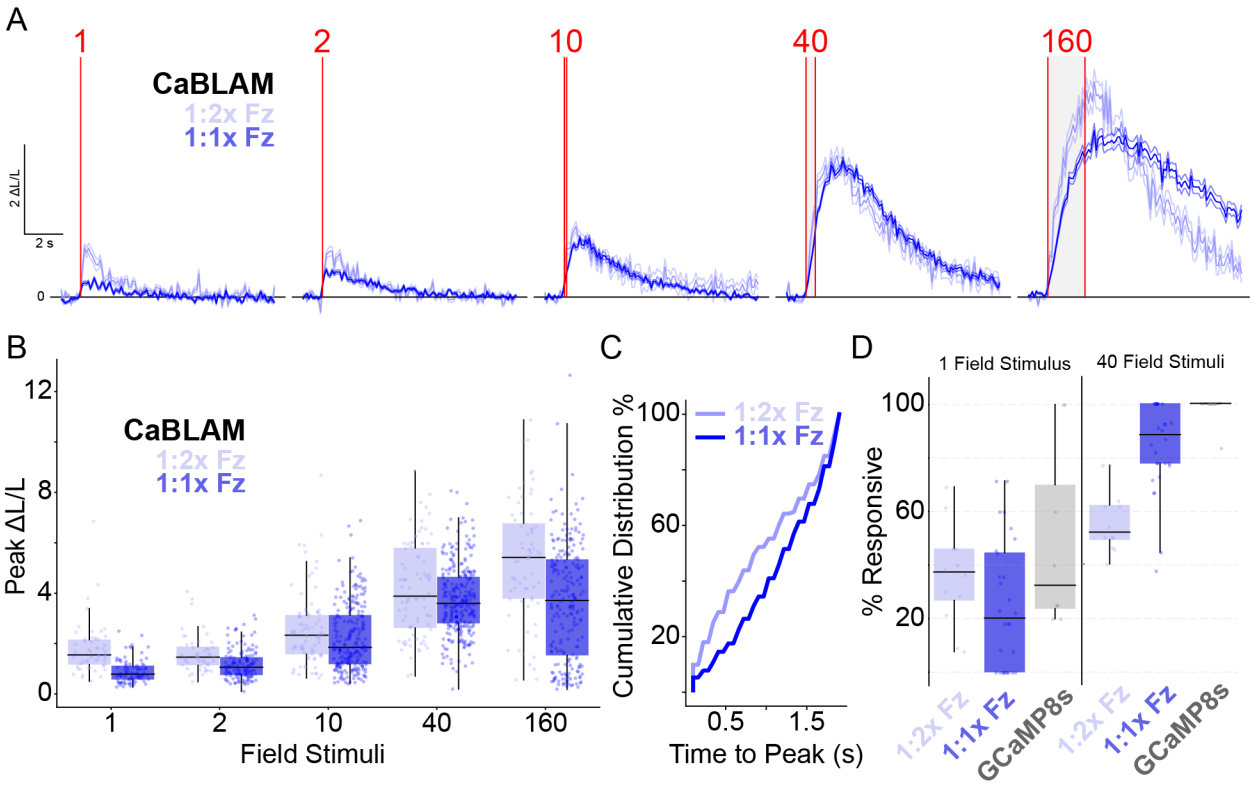

Figure 5. Decreasing furimazine (Fz) concentration leads to faster and larger evoked CaBLAM responses to a single electrical field stimulation. (A) Overlaid bioluminescence ΔL/L time-locked traces of CaBLAM calcium responses to 1, 2, 10, 40, 160 pulses of 1ms field stimulations at 83 Hz, at 1x (1:1) or ½ x (1:2) Fz concentration. Red dashed lines indicate field stimulation window. Data are shown as mean ± s.e.m. (B) Peak stimulus ΔL/L for CaBLAM across neurons elicited across increasing field stimulations in the presence of 1x (1:1) or ½ x (1:2) Fz. (C) Cumulative distribution of time to ΔL/L responses between (includes statistical analysis). (D) Proportion of neurons responding to 1 (left) and 40 (right) electrical field stimulations. For panel (B) and (D), boxplots show the median, 25th and 75th percentiles (box edges), whiskers extending to the most extreme data points, and individual outliers plotted separately.

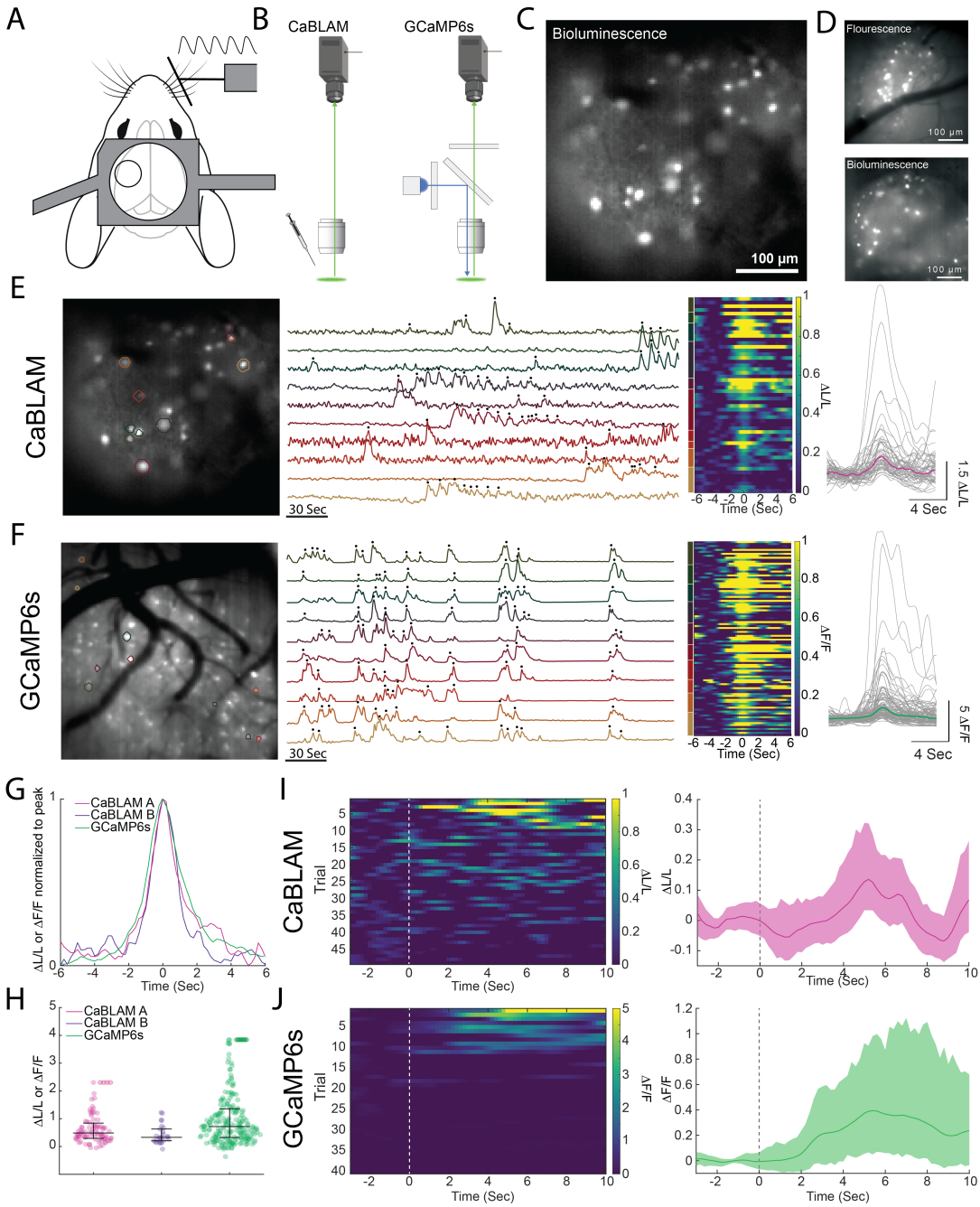

Figure 6. Imaging CaBLAM *in vivo*. (A) Illustration of the mouse imaging setup with location of the cranial window and steel headpost. (B) Basic comparison of the CaBLAM and GCaMP6s imaging setups. CaBLAM was imaged in darkness in a light tight enclosure after administration of the luciferin. GCaMP was imaged under epifluorescent illumination. (C) Example mean projection image of one CaBLAM animal. (D) In the same animal as (C), comparison of fluorescence versus bioluminescence in the same field of view. Flourescent and bioluminescent images were acquired on separate days. (E) Example data from one CaBLAM animal. From left to right: Mean projection image with 10 example ROIS plotted, timeseries plots of the same 10 ROIs with black dots indicating the locations of detected events, pseudo color image of detected calcium events across these 10 ROIs (colorbar on the left indicates which ROI each waveform belongs to), and plot of all detected calcium events (gray) and their median value (magenta). (F) Example data from the GCaMP6s mouse, same conventions as in (E). Note the y-axis of the waveforms on the far right is a different scale than the corresponding plot in (E). (G) Normalized median event waveforms for each of the three animals. (H) Peak df/f or dl/l for all events and all animals. Black bars represent the median peak value with whiskers extending to the 25th and 75th percentiles.

Peak values that extended beyond 3 times the interquartile range above the median are marked with red circles and plotted at the maximum peak not exceeding this threshold for illustration purposes only. (I) Example CaBLAM animal ROI response to vibrissa tactile stimulation (49 trials), left shows all trials aligned to stimulus onset. Right mean ROI timeseries across stimulus presentations. Opaque bars represent the bootstrapped 95% confidence intervals. (J) Same as in (I) but for the GCaMP6s animal. Note that the scaling is different between (I) and (J).

References

1. Shen, Y., Nasu, Y., Shkolnikov, I., Kim, A. & Campbell, R. E. Engineering genetically encoded fluorescent indicators for imaging of neuronal activity: progress and prospects. *Neurosci Res* **152**, 3–14 (2020).

2. Lin, M. Z. & Schnitzer, M. J. Genetically encoded indicators of neuronal activity. *Nat Neurosci* **19**, 1142–1153 (2016).

3. Hires, S. A., Tian, L. & Looger, L. L. Reporting neural activity with genetically encoded calcium indicators. *Brain Cell Biol* **36**, 69 (2008).

4. Dong, C. *et al.* Fluorescence Imaging of Neural Activity, Neurochemical Dynamics, and Drug-Specific Receptor Conformation with Genetically Encoded Sensors. *Annu. Rev. Neurosci.* **45**, 273–294 (2022).

5. Zhang, Y. *et al.* Fast and sensitive GCaMP calcium indicators for imaging neural populations. *Nature* **615**, 884–891 (2023).

6. Li, J. *et al.* Engineering of NEMO as calcium indicators with large dynamics and high sensitivity. *Nat Methods* 1–7 (2023) doi:10.1038/s41592-023-01852-9.

7. Doronin, D. A. *et al.* Genetically encoded calcium indicator with NTnC-like design and enhanced fluorescence contrast and kinetics. *Bmc Biotechnol* **18**, 10 (2018).

8. Dana, H. *et al.* Sensitive red protein calcium indicators for imaging neural activity. *eLife* **5**, 413 (2016).

9. Qian, Y. *et al.* Improved genetically encoded near-infrared fluorescent calcium ion indicators for in vivo imaging. *PLoS Biol.* **18**, e3000965 (2020).

10. Shimomura, O., Johnson, F. H. & SAIGA, Y. Extraction, purification and properties of aequorin, a bioluminescent protein from the luminous hydromedusan, Aequorea. *Journal of cellular and comparative physiology* **59**, 223–239 (1962).

11. Musicki, B., Kishi, Y. & Shimomura, O. Structure of the functional part of photoprotein aequorin. *Journal of the Chemical Society, Chemical Communications* 1566 (1986) doi:10.1039/c39860001566.

12. Naumann, E. A., Kampff, A. R., Prober, D. A., Schier, A. F. & Engert, F. Monitoring neural activity with bioluminescence during natural behavior. *Nature Neuroscience* **13**, 513–520 (2010).

13. Qian, Y., Rancic, V., Wu, J., Ballanyi, K. & Campbell, R. E. A Bioluminescent Ca2+ Indicator Based on a Topological Variant of GCaMP6s. *ChemBioChem* **20**, 516–520 (2019).

14. Farhana, I., Hossain, M. N., Suzuki, K., Matsuda, T. & Nagai, T. Genetically Encoded Fluorescence/Bioluminescence Bimodal Indicators for Ca 2+ Imaging. *Acs Sensors* **4**, 1825–1834 (2019).

15. Yang, J. *et al.* Coupling optogenetic stimulation with NanoLuc-based luminescence (BRET) Ca(++) sensing. *Nature communications* **7**, 13268 (2016).

16. Saito, K. *et al.* Luminescent proteins for high-speed single-cell and whole-body imaging. *Nature Communications* **3**, 1262 (2012).

17. Suzuki, K. *et al.* Five colour variants of bright luminescent protein for real-time multicolour bioimaging. *Nature Communications* **7**, 1–10 (2016).

18. Oh, Y. *et al.* An orange calcium-modulated bioluminescent indicator for non-invasive activity imaging. *Nat Chem Biol* **15**, 433–436 (2019).

19. Shimomura, O., Masugi, T., Johnson, F. H. & Haneda, Y. Properties and reaction mechanism of the bioluminescence system of the deep-sea shrimp Oplophorus gracilorostris. *Biochemistry* **17**, 994–998 (1978).

20. Inouye, S., Watanabe, K., Nakamura, H. & Shimomura, O. Secretional luciferase of the luminous shrimp Oplophorus gracilirostris: cDNA cloning of a novel imidazopyrazinone luciferase. *FEBS LETTERS* **481**, 19–25 (2000).

21. Inouye, S. & Sasaki, S. Overexpression, purification and characterization of the catalytic component of Oplophorus luciferase in the deep-sea shrimp, Oplophorus gracilirostris. *Protein Expression and Purification* **56**, 261–268 (2007).

22. Inouye, S., Sato, J., Sahara-Miura, Y., Yoshida, S. & Hosoya, T. Luminescence enhancement of the catalytic 19kDa protein (KAZ) of Oplophorus luciferase by three amino acid substitutions. *Biochemical and Biophysical Research Communications* **445**, 157–162 (2014).

23. Shaner, N. C. *et al.* A bright monomeric green fluorescent protein derived from Branchiostoma lanceolatum. *Nature Methods* **10**, 407–409 (2013).

24. Hall, M. P. *et al.* Engineered Luciferase Reporter from a Deep Sea Shrimp Utilizing a Novel Imidazopyrazinone Substrate. *ACS Chemical Biology* **7**, 1848–1857 (2012).

25. Dixon, A. S. *et al.* NanoLuc Complementation Reporter Optimized for Accurate Measurement of Protein Interactions in Cells. *ACS Chemical Biology* **11**, 400–408 (2015).

26. Förster, T. Zwischenmolekulare Energiewanderung Und Fluoreszenz. *Annalen Der Physik* **2**, 55–75 (1948).

27. Takai, A. *et al.* Expanded palette of Nano-lanterns for real-time multicolor luminescence imaging. *Proceedings of the National Academy of Sciences* **112**, 4352–4356 (2015).

28. Dana, H. *et al.* High-performance calcium sensors for imaging activity in neuronal populations and microcompartments. *Nat Methods* **16**, 649–657 (2019).

29. Chen, T.-W. *et al.* Ultrasensitive fluorescent proteins for imaging neuronal activity. *Nature* **499**, 295–300 (2013).

30. Mank, M. *et al.* A FRET-Based Calcium Biosensor with Fast Signal Kinetics and High Fluorescence Change. *Biophysical Journal* **90**, 1790–1796 (2006).

31. Palmer, A. E. *et al.* Ca2+ Indicators Based on Computationally Redesigned Calmodulin-Peptide Pairs. *Chemistry & Biology* **13**, 521–530 (2006).

32. Jensen, H. H., Brohus, M., Nyegaard, M. & Overgaard, M. T. Human Calmodulin Mutations. *Front. Mol. Neurosci.* **11**, 396 (2018).

33. Maravall, M., Mainen, Z. F., Sabatini, B. L. & Svoboda, K. Estimating Intracellular Calcium Concentrations and Buffering without Wavelength Ratioing. *Biophys. J.* **78**, 2655–2667 (2000).

34. Lovell, S. *et al.* 2.20A Resolution Structure of NanoLuc Luciferase with Bound Substrate Analog 3-methoxy-furimazine. (2022) doi:10.2210/pdb7snt/pdb.

35. Sauvé, R. *et al.* Ca2+ oscillations induced by histamine H1 receptor stimulation in HeLa cells: Fura-2 and patch clamp analysis. *Cell Calcium* **12**, 165–176 (1991).

36. Abs, E. *et al.* Learning-Related Plasticity in Dendrite-Targeting Layer 1 Interneurons. *Neuron* **100**, 684-699.e6 (2018).

37. Zenchak, J. R. *et al.* Bioluminescence-driven optogenetic activation of transplanted neural precursor cells improves motor deficits in a Parkinson's disease mouse model. *Journal of Neuroscience Research* **90**, 955 (2018).

38. Crespo, E. L. *et al.* Bioluminescent optogenetic (BL-OG) activation of neurons during mouse postnatal brain development. *Star Protoc* **2**, 100667 (2021).

39. Crespo, E. L., Bjorefeldt, A., Prakash, M. & Hochgeschwender, U. Bioluminescent Optogenetics 2.0: Harnessing Bioluminescence to Activate Photosensory Proteins In Vitro and In Vivo. *J Vis Exp* (2021) doi:10.3791/62850.

40. English, A. W. *et al.* Bioluminescent Optogenetics: A Novel Experimental Therapy to Promote Axon Regeneration after Peripheral Nerve Injury. *Int J Mol Sci* **22**, 7217 (2021).

41. Sureda-Vives, M. & Sarkisyan, K. S. Bioluminescence-Driven Optogenetics. *Life* **10**, 318 (2020).

42. Tung, J. K., Gutekunst, C.-A. & Gross, R. E. Inhibitory luminopsins: genetically-encoded bioluminescent opsins for versatile, scalable, and hardware-independent optogenetic inhibition. *Scientific Reports* **5**, 14366 (2015).

43. Petersen, E. D. *et al.* Restoring Function After Severe Spinal Cord Injury Through BioLuminescent-OptoGenetics. *Front Neurol* **12**, 792643 (2022).

44. Petersen, E. D. *et al.* Bioluminescent Genetically Encoded Glutamate Indicator for Molecular Imaging of Neuronal Activity. *Biorxiv* 2021.06.16.448690 (2021) doi:10.1101/2021.06.16.448690.

45. Gibson, D. G. *et al.* Enzymatic assembly of DNA molecules up to several hundred kilobases. *Nature Publishing Group* **6**, 343–345 (2009).

46. Lambert, G. G. *et al.* Aequorea's secrets revealed: New fluorescent proteins with unique properties for bioimaging and biosensing. *Plos Biol* **18**, e3000936 (2020).

47. Boassa, D. *et al.* Mapping the Subcellular Distribution of α-Synuclein in Neurons using Genetically Encoded Probes for Correlated Light and Electron Microscopy: Implications for Parkinson's Disease Pathogenesis. *J. Neurosci.* **33**, 2605–2615 (2013).

48. Berglund, K. *et al.* Luminopsins integrate opto- and chemogenetics by using physical and biological light sources for opsin activation. *Proceedings of the National Academy of Sciences of the United States of America* **113**, E358-67 (2016).

49. Wardill, T. J. *et al.* A neuron-based screening platform for optimizing genetically-encoded calcium indicators. *Plos One* **8**, e77728 (2013).

50. Pachitariu, M. & Stringer, C. Cellpose 2.0: how to train your own model. *Nat. Methods* **19**, 1634–1641 (2022).

51. Schuman, B. *et al.* Four Unique Interneuron Populations Reside in Neocortical Layer 1. *J. Neurosci.* **39**, 125–139 (2019).

52. Lu, J. *et al.* MIN1PIPE: A Miniscope 1-Photon-Based Calcium Imaging Signal Extraction Pipeline. *Cell Rep.* **23**, 3673–3684 (2018).